Adatom-driven oxygen intermixing during the deposition of oxide thin films by molecular beam epitaxy

Journal:	*Nano Letters*
Manuscript ID	nl-2022-01678h.R2
Manuscript Type:	Communication
Date Submitted by the Author:	n/a
Complete List of Authors:	Kaspar, Tiffany ; Pacific Northwest National Laboratory, Hatton, Peter; Los Alamos National Laboratory Yano, Kayla; Pacific Northwest National Laboratory, Energy and Environment Taylor, Sandra; Pacific Northwest National Laboratory, Geochemistry Spurgeon, Steven; Pacific Northwest National Laboratory, Energy and Environment Directorate Uberuaga, Blas; Los Alamos National Laboratory, Schreiber, Daniel; Pacific Northwest National Laboratory,

Adatom-driven oxygen intermixing during the deposition of oxide thin films by molecular beam epitaxy

Tiffany C. Kaspar[1,], Peter Hatton[2], Kayla H. Yano[3], Sandra D. Taylor[1], Steven R. Spurgeon[3,4], Blas P. Uberuaga[2,*], Daniel K. Schreiber[3]*

[1]Physical and Computational Sciences Directorate, Pacific Northwest National Laboratory, Richland, WA 99354, USA

[2]Material Science and Technology Division, Los Alamos National Laboratory, Los Alamos, New Mexico 87545, USA

[3]Energy and Environment Directorate, Pacific Northwest National Laboratory, Richland, WA 99354, USA

[4]Department of Physics, University of Washington, Seattle, WA 98195, USA

Corresponding Authors

Tiffany C. Kaspar - Physical and Computational Sciences Directorate, Pacific Northwest National Laboratory, Richland, WA 99354, United States; orcid.org/0000-0003-2816-7569; tiffany.kaspar@pnnl.gov

Blas P. Uberuaga - Material Science and Technology Division, Los Alamos National Laboratory, Los Alamos, New Mexico 87545, United States; orcid.org/0000-0001-6934-6219; blas@lanl.gov

ABSTRACT

Thin film deposition from the vapor phase is a complex process involving adatom adsorption, movement, and incorporation into the growing film. Here we present quantitative experimental data that reveals anion intermixing over long length scales during the deposition of epitaxial Fe_2O_3 and Cr_2O_3 films and heterostructures by oxygen-plasma-assisted molecular beam epitaxy. We track this diffusion by incorporating well-defined tracer layers containing ^{18}O and/or ^{57}Fe, and measure their redistribution on the nanometer scale with atom probe tomography. Molecular dynamics simulations suggest potential intermixing events, which are then examined via nudged elastic band calculations. We reveal that adatoms on the film surface act to "pull up" subsurface O and Fe. Subsequent ring-like rotation mechanisms involving both adatom and subsurface anions

then facilitate their mixing. In addition to film deposition, these intermixing mechanisms may be operant during other surface-mediated processes such as heterogeneous catalysis and corrosion.

KEYWORDS Hematite, diffusion, molecular beam epitaxy, interface abruptness, surface exchange

Thin film deposition from the vapor phase is a key technology that enables both commercial fabrication for a wide variety of applications and the research and development of new materials and devices for next-generation technologies. Despite its importance, a comprehensive, predictive understanding of the thin film deposition process is still lacking. Thin film morphology during well-controlled, non-energetic deposition (by molecular beam epitaxy (MBE), for example) is understood as a competition between surface and interface energies, tempered by adatom mobility, leading to the well-known layer-by-layer (Frank-van der Merwe), layer-island (Stranski-Krastanov), and 3D island (Volmer-Weber) growth modes. [1-2] These growth modes can be modeled considering only surface dynamics that dictate adatom motion. Even very recent modeling efforts[3-5] must neglect any subsurface or bulk diffusion of species during the deposition process to keep the simulations tractable. These models provide insight into the development of thin film morphology by estimating energy barriers for adatom processes such as adsorption, surface diffusion, and desorption. However, it is well understood by the thin film growth community that interlayer diffusion and intermixing often accompanies film deposition, [6-9] and that this interlayer transport cannot be explained by simple bulk lattice diffusion at the deposition temperature.

It is critical to understand the interlayer diffusion and intermixing processes occurring during thin film deposition to tailor the atomically precise deposition of functional materials and heterostructures. More broadly, surface-mediated intermixing and atom exchange processes can play a significant role in heterogeneous catalysis[10] and corrosion, [11-12] such that understanding the chemical driving forces for these processes is key to designing next-generation materials with desired properties. Recent modeling efforts have begun to address this challenge. Lloyd *et al.* [13] simulated metal and metal oxide deposition with adaptive kinetic Monte Carlo and observed concerted atom motions driven by adatom adsorption that, in some cases, resulted in atom exchange with the underlying layer. Zhou *et al.* [14] used elevated temperature molecular dynamics (MD) simulations to model the deposition of Ge on Si, and found energetically favorable atomic motions resulting in both Ge substitution for Si in the initial stage of film growth, resulting in intermixing in agreement with experimental observations, [6] and in later stages of film growth, concerted atom motions occur as Ge adatoms attach to the bottom of growing Ge pyramids, pushing other Ge atoms to "climb" the pyramid. In both these studies, the observed concerted atom motions appear to be driven by chemical effects, not simple bulk lattice diffusion.

In this paper, we provide insight into the mechanisms governing cation and anion intermixing during vapor deposition. To avoid any thermodynamic preference for diffusion across interfaces, we study self-diffusion in the simple binary oxides Cr_2O_3 and Fe_2O_3, building on our previous observation of $^{16}O/^{18}O$ intermixing when a layer of $M_2{}^{18}O_3$ (M = Fe, Cr) is included in epitaxial thin films deposited by molecular beam epitaxy. [15] These interlayer exchange mechanisms are operant on the anion sublattice to a more significant degree than previously appreciated, and the resultant intermixing can be both visualized and quantified using the powerful synthesis and characterization methods we employ here. Adatom deposition is simulated with MD, and the underlying atomic processes leading to intermixing are elucidated by using the complex results of these simulations to inform static calculations of energy barriers and intermixing pathways. We observe facile concerted atom motions that lead to intermixing, driven by the presence of adatoms on the film surface. By comparing to experimental isotopic tracer concentration profiles, we provide preliminary estimates of the extent of these intermixing events.

Cation and anion diffusion and intermixing during the epitaxial deposition of hematite, α-Fe_2O_3, and eskolaite, Cr_2O_3, on Al_2O_3(0001) at 730˚C by ion-filtered, oxygen-plasma-assisted

molecular beam epitaxy (OPA-MBE) is observed by including a well-defined, 5 - 10 nm thick $Cr_2{}^{18}O_3$ or $^{57}Fe_2{}^{18}O_3$ tracer layer within the film and quantifying the resulting isotopic tracer concentration profiles with atom probe tomography (APT) (see Methods in the SI for details). To quantify the role of oxygen mobility in the lattice on intermixing, epitaxial Cr_2O_3 / $Cr_2{}^{18}O_3$ / M_2O_3 / Al_2O_3 film stacks (M = Al, Cr, Fe) were synthesized. As sketched in Fig. 1a, the epitaxial material between the $Cr_2{}^{18}O_3$ tracer and the Al_2O_3 substrate is either Al_2O_3 (*i.e.*, tracer layer deposition directly on the substrate), 100 nm Fe_2O_3, or 50 nm Cr_2O_3. All three film stacks are capped with Cr_2O_3 (60 nm for M = Al, Cr; 25 nm for M = Fe). In all three cases, both the average and the peak ^{18}O enrichment in the $Cr_2{}^{18}O_3$ tracer layer is less than the $^{18}O_2$ source (99% enrichment). As illustrated by the ^{18}O concentration profile data in Fig. 1a, the level of enrichment in the tracer layer decreases dependent on the underlying material: Fe_2O_3 < Cr_2O_3 < Al_2O_3. Comparing the predicted anion diffusivity of the underlying M_2O_3 layer at 730˚C indicates that the tracer layer enrichment decreases with increasing anion mobility: 5×10^{-19} cm^2 s^{-1} for Fe_2O_3[16] > 2×10^{-21} cm^2 s^{-1} for Cr_2O_3[17] > 3×10^{-31} cm^2 s^{-1} for Al_2O_3.[18]

A similar reduction in ^{18}O enrichment is observed for $Fe_2{}^{18}O_3$, as shown in Fig. 1b. The anion diffusion data for Fe_2O_3 in Fig. 1b illustrates that enrichment of the tracer layer is also

correlated with deposition rate: slower deposition rate (*i.e.*, longer time required to deposit a 10 nm thick layer) leads to lower enrichment. As detailed previously, [15] altering the growth protocol (such as increasing the time that the residual natural abundance (NA) O is pumped out before the introduction of ^{18}O) does not increase the ^{18}O enrichment in the layer.

For both Cr_2O_3 and Fe_2O_3, increasing enrichment is observed from the bottom to the top of the tracer layer, leading to a characteristic negative slope to the ^{18}O profile within the tracer layer (as examples, see the solid black lines in Fig. 1a). In addition, the ^{18}O profile in the upper, NA Cr_2O_3 or Fe_2O_3 layer decreases slowly but does not reach the NA value of 0.2% (in contrast, the ^{18}O level in the lower NA layer is ~0.2%). Neither the reduction in enrichment in the tracer layers nor the ^{18}O persistence in the upper film is predicted by thermally-activated bulk lattice diffusion: the gray lines in Fig. 1a and b are predicted ^{18}O profiles calculated from Fick's Law[19-20] assuming diffusion coefficients extrapolated from high temperature experimental data for Cr_2O_3[17] and Fe_2O_3.[16] The predicted anion diffusion for Cr_2O_3 at 730˚C for 4 h is minor, in contrast to the observed ^{18}O redistribution observed experimentally in Fig. 1a. Somewhat more anion diffusion is predicted for Fe_2O_3 under the same conditions, but the tracer redistribution is still far less than that observed experimentally in Fig. 1b.

The behavior of ^{57}Fe in $^{57}Fe_2{}^{18}O_3$ in Fig. 1c is markedly different than the anion behavior shown in Fig. 1a and b; the ^{57}Fe cations follow the predicted bulk lattice diffusion profile reasonably closely. The peak cation enrichment in the tracer layer is measured to be approximately the same as the enrichment of the ^{57}Fe source, ~95% ^{57}Fe. In addition, no characteristic negative slope is observed in the ^{57}Fe profile within the tracer layer. Very slight deviations from the thermally-activated bulk lattice diffusion behavior predicted by Fick's Law are observed: although the measured ^{57}Fe diffusion profile width matches the Fick's law prediction (within experimental error), the profile is slightly asymmetric to the upper side of the tracer layer (red arrow in Fig. 1c). The ^{57}Fe concentration then falls quickly to the NA value of 2.2%.

The anion tracer diffusion behavior observed experimentally in Fig. 1 cannot be explained within the simplified framework of epitaxial thin film growth mechanisms, where minimal interaction of the adatoms with the underlying film is presumed. Instead, we suggest that these experimental results can only be reconciled if significant intermixing of the first one or few layers of the film occurs at the growth front, driven not by bulk lattice diffusion but by the arriving adatoms from the vapor phase. To elucidate the possible mechanisms that might be

operable at the growth surface that would be responsible for this intermixing, we performed molecular dynamics (MD) simulations. An MD simulation was conducted which simulated the deposition process of Fe_2O_3 on Fe_2O_3(0001) with an initial slab thickness of 1.28 nm, using conventional MD and Parallel Replica Dynamics (ParRep) [21] (see Methods in the SI for further details). The development of a non-crystalline surface morphology in this simulation, as well as the density of adatoms in the vicinity of intermixing events and strong interactions between adatoms and near-surface layers, means it is difficult to meaningfully visualize and extract the O intermixing events which took place. Therefore, the result of the MD/ParRep simulation is not shown in this work; rather, the intermixing events which did take place during this simulation were used as motivation for static nudged elastic band (NEB) calculations of intermixing events, which will be presented and discussed.

Firstly, we observed that adatoms on the Fe_2O_3(0001) surface have strong interactions with atoms in the first layer and can "pull up" atoms onto the surface. This can allow intermixing pathways to become available, leading to ^{18}O moving from the surface into the first layer and second layer of Fe_2O_3. This is perhaps the most critical observation from our modeling, as it is these "pull up" processes that often catalyze the subsequent behavior.

Figure 2a outlines this process for first layer mixing when 1 Fe and 1 O deposit onto the surface. The first part of the process shows the result of adding a single ^{18}O to the surface (event I). An ^{16}O and Fe are both pulled from the surface, creating near-surface vacancies. These can be "repaired" by the addition of a second Fe atom on the surface (event II), which induces an O close to the vacancy to move and fill it. This could in theory be either an ^{16}O or ^{18}O depending on the configuration of adatoms at that time, and therefore event II could be a source of ^{18}O replacement/mixing in the first layer.

With this optimal surface configuration of 1 Fe and 1 ^{18}O adatom, a ring-like rotation of the ^{18}O adatom and two first layer ^{16}O oxygens can occur (event III in Fig. 2a), resulting in an ^{16}O adatom on the surface and an ^{18}O in the first layer. The NEB calculations of the energetic barriers for this mechanism can be seen in Figure 2c, as well as the barrier calculated with a sub-optimal surface structure of just a single ^{18}O. The more favorable case has a barrier of 1.2 eV, and this barrier approximately doubles if the Fe adatom is not included (single ^{18}O adatom only). The relative energy change between the initial and final state for these mechanisms is 0.0 eV, meaning that we would expect this rotational barrier, the barrier required to perform the ring-like rotation of the ^{18}O adatom and two first layer ^{16}O, to reverse with the same rate, and therefore the

^{18}O will churn between the surface and the first layer until presumably a new adatom surface configuration locks this pathway. We also find that adatoms are relatively immobile on the surface, with O encountering ~ 2 eV barriers to move across the surface.

Figure 2b shows the process for intermixing of an ^{18}O from the first layer of Fe_2O_3 to the second layer. A deposited cluster of 1 Fe and 2 ^{18}O adatoms on the surface results in the "pulling up" of an ^{16}O and an Fe (event I). This surface configuration allows for a ring-like rotation mechanism to occur (event II), with the net result of an ^{18}O moving from the first to the second layer and the concurrent pulling of an ^{16}O to the surface. The barrier for this process, shown in Figure 2d (1 Fe 2 O case) alongside similar processes with less optimal surface configurations, is just slightly over 1 eV. Note that increasing the number of surface adatoms decreases the energy barrier from a prohibitively high barrier of 5 eV with a clean surface to a minimum of 1 eV, emphasizing the role of the surface adatoms and the induced subsurface vacancies in catalyzing the mixing.

The most striking aspect of this mixing event, with the optimal surface structure, is the corresponding 3 eV energy decrease after the ring-like rotation. This energy change implies that second layer intermixing of ^{18}O with this surface morphology is no longer a process that is

equally likely to undo itself, but instead the ^{18}O is driven to the second layer. This is due to the creation of near-surface vacancies caused by the pulling up of near-surface atoms by the surface adatoms, as previously described.

Turning our attention to cation intermixing, upon close inspection of our initial MD/ParRep simulation, we found that in the 300 ns simulation time three Fe atoms moved from the surface layer into the first layer, compared to a total of 16 O atoms. The complexity of the structure which led to this mixing has made it difficult to isolate the mechanisms responsible for it; however, we have identified this move as the result of Fe atoms from the surface filling near-surface vacancies that are created by the presence of the adatoms, as previously discussed in Figure 2.

To assess whether the mechanisms of mixing described above are enough to fully explain the $^{18}O/^{16}O$ distribution seen experimentally, we present a simple model of the intermixing process. As neither the rate nor barrier is accurately known for Fe mixing, the model focuses on O mixing only. Figure 3a schematically describes the model process. At step *i*, three atomic layers of O are actively swapped, atom by atom, a total of 10^5 times. This number of swaps is close to the number of exchanges we would expect at experimental timescales, as estimated by

the deposition rate (0.24 Å s^{-1}), and our calculated barriers (see Methods in the SI for details). After 10^5 swaps, a full layer is then added to the surface and the process moves up to this next layer, essentially freezing the bottom layer (meaning no swaps occur in layers outside of this set, which removes consideration of bulk diffusion). To approximately reproduce the experimental film stacks shown in Fig. 1, ^{16}O layers were added first until a thickness of ~5.2 nm was reached, then a subsequent ~6.9 nm of ^{18}O layers were added before a final ~8.5 nm of ^{16}O, resulting in a 20.6 nm sample.

Figure 3b shows the result of the ^{18}O distribution analysis, and Fig. 3d shows the actual structure at the end of the simulation. It is clear that, while mixing has occurred, the mixed region quickly diminishes to zero before the full 10 nm $Fe_2{}^{18}O_3$ region has ended. This does not agree well with the experimental analysis, which shows that there is ^{16}O contribution throughout the $Fe_2{}^{18}O_3$ region of the sample (Fig. 1b).

We have identified some reasons why the simple model employed may not be able to accurately reproduce the ^{18}O distributions observed in experiment, focusing on the simplicity and assumptions of the model. For example, the asymmetry of the second layer mixing barrier shown in Figure 2d is not captured in this model. The model simply swaps O from each layer randomly

without consideration of the thermodynamic effects of this swapping, and thus each swap is equally likely to be undone. The actual surface structure and the thermodynamic driving forces of the subsurface vacancies may drive and stabilize more intermixing than assumed here. Similarly, the layer-by-layer growth simulated here is artificial and may not capture intermediate surface structures which may block mixing after some time, leading to our model "churning" more O than in reality. Lastly, we have computational evidence to support a 3-layer mixing model but it may be that deeper mixing is possible. For example, if we postulate a 7-layer mixing model, the results of which can be seen in Figure 3c and e, then a ^{18}O distribution quantitatively similar to that observed experimentally for $Cr_2{}^{18}O_3$ buried in Cr_2O_3 is obtained. The simulated ^{18}O distribution also shares qualitative features (such as profile shape and asymmetry) with the experimental ^{18}O profile from $Fe_2{}^{18}O_3$ buried in Fe_2O_3 at a deposition rate of 0.1 Å/s.

The experimental results indicate that there is less intermixing in Cr_2O_3 than in Fe_2O_3. The mechanisms identified for intermixing of ^{18}O in Fe_2O_3 were thus used to conduct a similar study of intermixing in Cr_2O_3, using only optimal adatom configurations to calculate barriers. We find that, in Cr_2O_3, first layer mixing of ^{18}O has a barrier of 1.6 eV, compared to 1.2 eV in Fe_2O_3. The barrier for second layer mixing is approximately the same as in Fe_2O_3, 1 eV, in

Cr_2O_3, though there is a smaller secondary barrier of 0.7 eV, revealing a more complex landscape. Both mechanisms will result in less mixing of O due to analogous but slower pathways in Cr_2O_3, consistent with the experiments.

The extent of anion intermixing observed during the deposition of epitaxial Fe_2O_3 and Cr_2O_3 thin films by OPA-MBE is significant compared to the expected bulk lattice diffusion at the deposition temperature. In addition, this intermixing was found to be asymmetric, with an increase in ^{18}O in the layer above the isotopically labeled layer and a corresponding increase in ^{16}O from the layer below into the isotopically labeled layer. Our molecular dynamics simulations reveal that this asymmetry can be attributed to surface adatoms "pulling up" subsurface cations and anions. A similar mechanism was found for rutile $TiO_2(110)$, with an adsorbed O_2 reducing the barrier for an interstitial Ti to move to the surface. [13] In the case of Fe_2O_3, however, the O adatom reduces the barrier for subsurface lattice atoms to move to the surface, and thus does not rely on the presence of defects such as interstitials. The ring-like rotation mechanisms we have identified that serve to mix anions between the surface and subsurface layers are predicted to be facile, leading to the larger-scale intermixing observed experimentally. In the many classes of oxides with higher anion and cation mobility than the

corundum-structure oxides, bulk diffusion is likely to become non-negligible during the deposition. However, we hypothesize that the surface-mediated intermixing mechanisms that we propose here will still be operant, and (depending on energetic barriers) may still dominate over bulk diffusion. In addition, these surface-mediated anion (and, to a lesser extent, cation) exchange mechanisms are expected to impact heterogeneous catalysis and corrosion processes in addition to vapor-phase thin film deposition.

ASSOCIATED CONTENT

Supporting Information

The Supporting Information is available free of charge at

Details of the synthesis, atom probe tomography analysis, computational simulations, and the motivation for the model using 10^5 exchanges per layer (PDF)

AUTHOR INFORMATION

Notes

The authors declare no competing financial interests.

ACKNOWLEDGMENT

This work was supported as part of FUTURE (Fundamental Understanding of Transport Under Reactor Extremes), an Energy Frontier Research Center funded by the U.S. Department of Energy (DOE), Office of Science, Basic Energy Sciences. A portion of the research was performed using EMSL (grid.436923.9), a DOE Office of Science User Facility sponsored by the Biological and Environmental Research program and located at Pacific Northwest National Laboratory. Pacific Northwest National Laboratory is a multi-program national laboratory operated by Battelle for the U.S. DOE under Contract DE-AC05-79RL01830. Los Alamos National Laboratory, an affirmative action equal opportunity employer, is managed by Triad National Security, LLC for the U.S. Department of Energy's NNSA, under contract 89233218CNA000001.

REFERENCES

(1) Ratsch, C.; Venables, J. A. Nucleation theory and the early stages of thin film growth. *Journal of Vacuum Science & Technology A* **2003,** *21* (5), S96-S109.

(2) Venables, J. A.; Spiller, G. D. T.; Hanbucken, M. Nucleation and Growth of Thin-Films. *Rep. Prog. Phys.* **1984,** *47* (4), 399-459.

(3) Empting, E.; Klopotek, M.; Hinderhofer, A.; Schreiber, F.; Oettel, M. Lattice gas study of thin-film growth scenarios and transitions between them: Role of substrate. *Physical Review E* **2021,** *103* (2), 023302.

(4) Luis, E. E. M.; Carrasco, I. S. S.; de Assis, T. A.; Reis, F. Statistics of adatom diffusion in a model of thin film growth. *Physical Review E* **2020,** *102* (1), 012805.

(5) To, T. B. T.; Almeida, R.; Ferreira, S. O.; Reis, F. Roughness and correlations in the transition from island to film growth: Simulations and application to CdTe deposition. *Appl. Surf. Sci.* **2021,** *560*, 149946.

(6) Uberuaga, B. P.; Leskovar, M.; Smith, A. P.; Jonsson, H.; Olmstead, M. Diffusion of Ge below the Si(100) surface: Theory and experiment. *Phys. Rev. Lett.* **2000,** *84* (11), 2441-2444.

(7) Chambers, S. A.; Engelhard, M. H.; Shutthanandan, V.; Zhu, Z.; Droubay, T. C.; Qiao, L.; Sushko, P. V.; Feng, T.; Lee, H. D.; Gustafsson, T.; Garfunkel, E.; Shah, A. B.; Zuo, J. M.; Ramasse, Q. M. Instability, intermixing and electronic structure at the epitaxial LaAlO3/SrTiO3(001) heterojunction. *Surf. Sci. Rep.* **2010,** *65* (10-12), 317-352.

(8) Posadas, A. B.; Kwon, S.; Christensen, A.; Kim, M. J.; Demkov, A. A. Facile growth of epitaxial vanadium monoxide on SrTiO3 via substrate oxygen scavenging. *Journal of Vacuum Science & Technology A* **2022,** *40* (1), 013416.

(9) Gao, Y.; Kim, Y. J.; Chambers, S. A. Preparation and characterization of epitaxial iron oxide films. *J. Mater. Res.* **1998,** *13* (7), 2003-2014.

(10) Vedrine, J. C. Heterogeneous Catalysis on Metal Oxides. *Catalysts* **2017,** *7* (11), 341.

(11) Maurice, V.; Marcus, P. Progress in corrosion science at atomic and nanometric scales. *Prog. Mater. Sci.* **2018,** *95*, 132-171.

(12) Schmidt, F.; Hosemann, P.; Scarlat, R. O.; Schreiber, D. K.; Scully, J. R.; Uberuaga, B. P., Effects of Radiation-Induced Defects on Corrosion. In *Annual Review of Materials Research, Vol 51, 2021*, Clarke, D. R., Ed. 2021; Vol. 51, pp 293-328.

(13) Lloyd, A. L.; Zhou, Y.; Yu, M.; Scott, C.; Smith, R.; Kenny, S. D. Reaction pathways in atomistic models of thin film growth. *Journal of Chemical Physics* **2017,** *147* (15), 152719.

(14) Zhou, Y.; Lloyd, A.; Smith, R.; Lozovoy, K. A.; Voitsekhovskii, A. V.; Kokhanenko, A. P. Molecular dynamics simulations of the growth of Ge on Si. *Surf. Sci.* **2020,** *696*, 121594.

(15) Kaspar, T. C.; Taylor, S. D.; Yano, K. H.; Lach, T. G.; Zhou, Y.; Zhu, Z.; Kohnert, A. A.; Still, E. K.; Hosemann, P.; Spurgeon, S. R.; Schreiber, D. K. Bulk and Short-Circuit Anion Diffusion in Epitaxial Fe_2O_3 Films Quantified Using Buried Isotopic Tracer Layers. *Advanced Materials Interfaces* **2021,** *8*, 2001768.

(16) Reddy, K. P. R.; Cooper, A. R. Oxygen Diffusion in MgO and α-Fe_2O_3. *J. Am. Ceram. Soc.* **1983,** *66* (9), 664-666.

(17) Hagel, W. C. Anion Diffusion in a-Cr_2O_3. *J. Am. Ceram. Soc.* **1965,** *48* (2), 70.

(18) Reddy, K. P. R.; Cooper, A. R. Oxygen Diffusion in Sapphire. *J. Am. Ceram. Soc.* **1982,** *65* (12), 634-638.

(19) Crank, J., *The Mathematics of Diffusion*. Clarendon Press: Oxford, 1975.

(20) Kiga, R.; Hayashi, S.; Miyamoto, S.; Shimizu, Y.; Nagai, Y.; Endoh, T.; Itoh, K. M. Oxidation-Enhanced Si Self-Diffusion in Isotopically Modulated Silicon Nanopillars. *J. Appl. Phys.* **2020,** *127* (4), 045704.

(21) Voter, A. F. Parallel replica method for dynamics of infrequent events. *Phys. Rev. B* **1998,** *57* (22), 13985-13988.

FIGURE CAPTIONS

Figure 1. ^{18}O concentration profiles plotted on a linear scale (left) and log scale (right) for (a) Cr_2O_3 and (b) Fe_2O_3 epitaxial thin film stacks. The inset of (a) sketches the stack sequence, consisting of either 5 nm (green curve) or 10 nm (blue curves) of ^{18}O-enriched $Cr_2{}^{18}O_3$ deposited onto different underlying materials of Al_2O_3, Cr_2O_3, or Fe_2O_3 (see legend), and each capped with Cr_2O_3. Solid black lines in (a) indicate the negative slope of the ^{18}O profile in the tracer layer. (c) ^{18}O and ^{57}Fe concentration profiles for Fe_2O_3 epitaxial thin film stack. Red arrow indicates ^{57}Fe profile asymmetry. Solid and dotted gray lines in all panels are predicted tracer diffusion profiles assuming bulk lattice diffusion at 730˚C for 4 h. Horizontal dashed (^{18}O) and dotted (^{57}Fe) lines indicate natural abundance of these isotopes.

Figure 2. (a,b) Mechanisms and surface structures that lead to ^{18}O intermixing from (a) the surface to the first layer and (b) from the first layer to the second. The mechanism that results in the lowest barrier is shown. Those atoms moving more than 1 Å during the event are highlighted, with the direction of motion indicated both by the shade of color and the size of the sphere (dark/small indicate initial position while light/large indicate final position). The schematic highlights both the

surface configuration of adatoms, particularly how the deposition process catalyzes the formation of further adatoms and subsurface defects, and the nature of the defects thus generated. (c,d) NEB results of energy barriers with differing surface adatoms for (c) surface to first layer mixing and (d) first layer to second layer mixing. The legend indicates what surface adatoms were present in those specific NEB calculations. The cases that are highlighted in (a) and (b) are also noted in the legend.

Figure 3. (a) Schematic of model mixing algorithm. As new layers are added to the growth front (after 100k swaps for the previous step), the active region (the surface and sub-surface) moves up one layer. The layers underneath are then considered frozen and all oxygen in those layers remain in place for the duration of the simulation. (b,c) ^{18}O distribution results from the model with (b) 3 layers mixing and (c) 7 layers mixing, as well as experimental ^{18}O distributions in $Fe_2O_3/Fe_2{}^{18}O_3/Fe_2O_3$ (0.1 Å/s) and $Cr_2O_3/Cr_2{}^{18}O_3/Cr_2O_3$. (d-e) The resulting atomistic profiles from the (d) 3 layer and (e) 7 layer model. Green: ^{18}O, Blue: ^{16}O. The bar indicates the isotope of oxygen that is "deposited" when a new layer is added at that point in the simulation. For clarity,

larger spheres indicate atoms that mixed into a region of the other isotope, while the atoms of the deposited isotope are displayed as smaller spheres. Fe atoms are not shown.

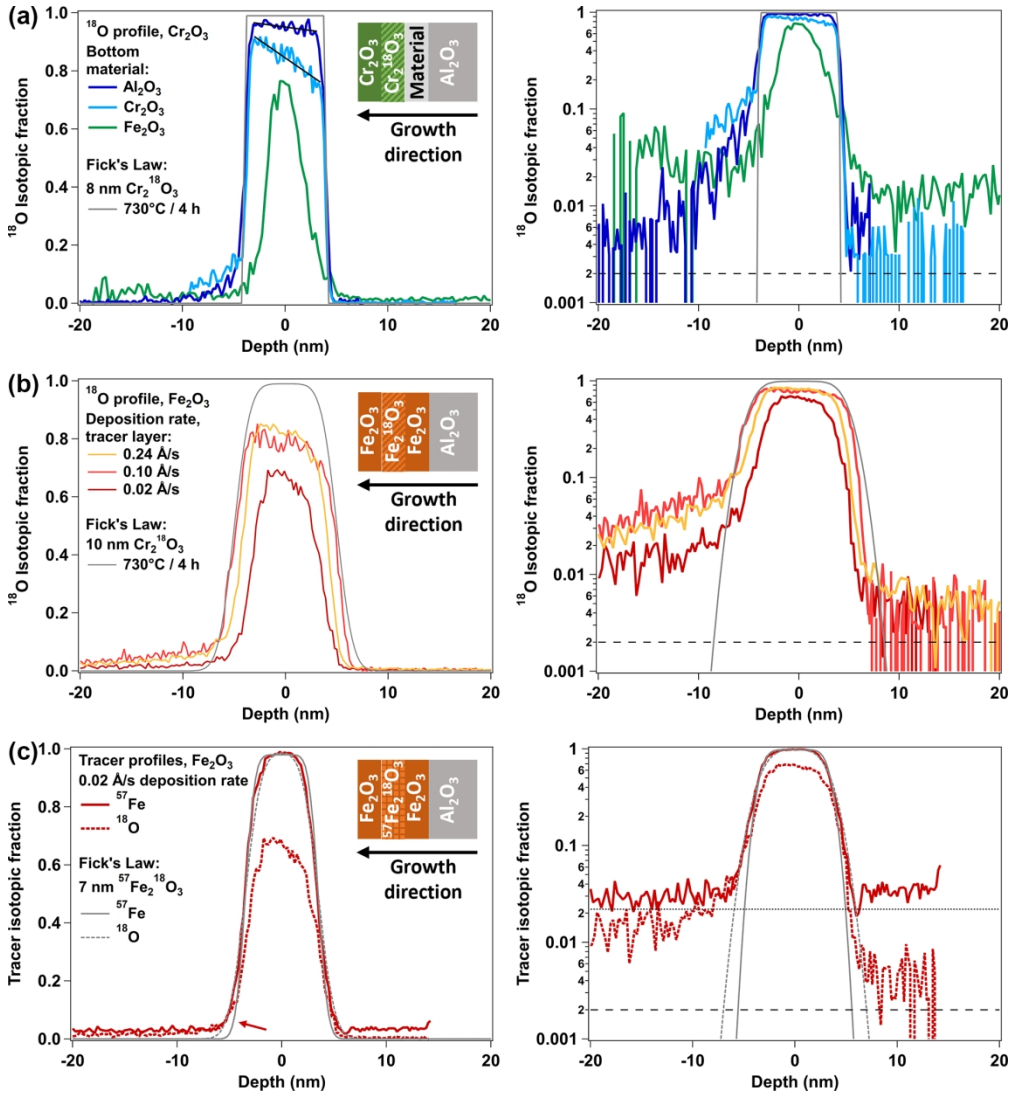

Figure 1. ^{18}O concentration profiles plotted on a linear scale (left) and log scale (right) for (a) Cr_2O_3 and (b) Fe_2O_3 epitaxial thin film stacks. The inset of (a) sketches the stack sequence, consisting of either 5 nm (green curve) or 10 nm (blue curves) of ^{18}O-enriched $Cr_2{}^{18}O_3$ deposited onto different underlying materials of Al_2O_3, Cr_2O_3, or Fe_2O_3 (see legend), and each capped with Cr_2O_3. Solid black lines in (a) indicate the negative slope of the ^{18}O profile in the tracer layer. (c) ^{18}O and ^{57}Fe concentration profiles for Fe_2O_3 epitaxial thin film stack. Red arrow indicates ^{57}Fe profile asymmetry. Solid and dotted gray lines in all panels are predicted tracer diffusion profiles assuming bulk lattice diffusion at 730°C for 4 h. Horizontal dashed (^{18}O) and dotted (^{57}Fe) lines indicate natural abundance of these isotopes.

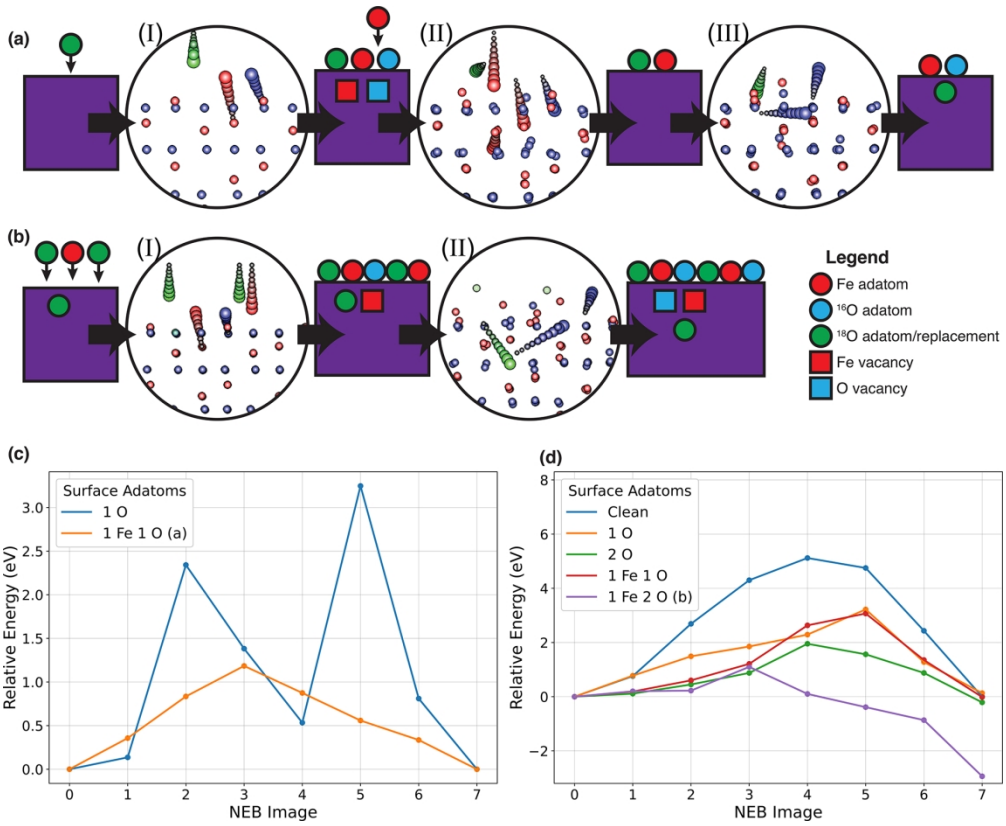

Figure 2. (a,b) Mechanisms and surface structures that lead to ^{18}O intermixing from (a) the surface to the first layer and (b) from the first layer to the second. The mechanism that results in the lowest barrier is shown. Those atoms moving more than 1 Å during the event are highlighted, with the direction of motion indicated both by the shade of color and the size of the sphere (dark/small indicate initial position while light/large indicate final position). The schematic highlights both the surface configuration of adatoms, particularly how the deposition process catalyzes the formation of further adatoms and subsurface defects, and the nature of the defects thus generated. (c,d) NEB results of energy barriers with differing surface adatoms for (c) surface to first layer mixing and (d) first layer to second layer mixing. The legend indicates what surface adatoms were present in those specific NEB calculations. The cases that are highlighted in (a) and (b) are also noted in the legend.

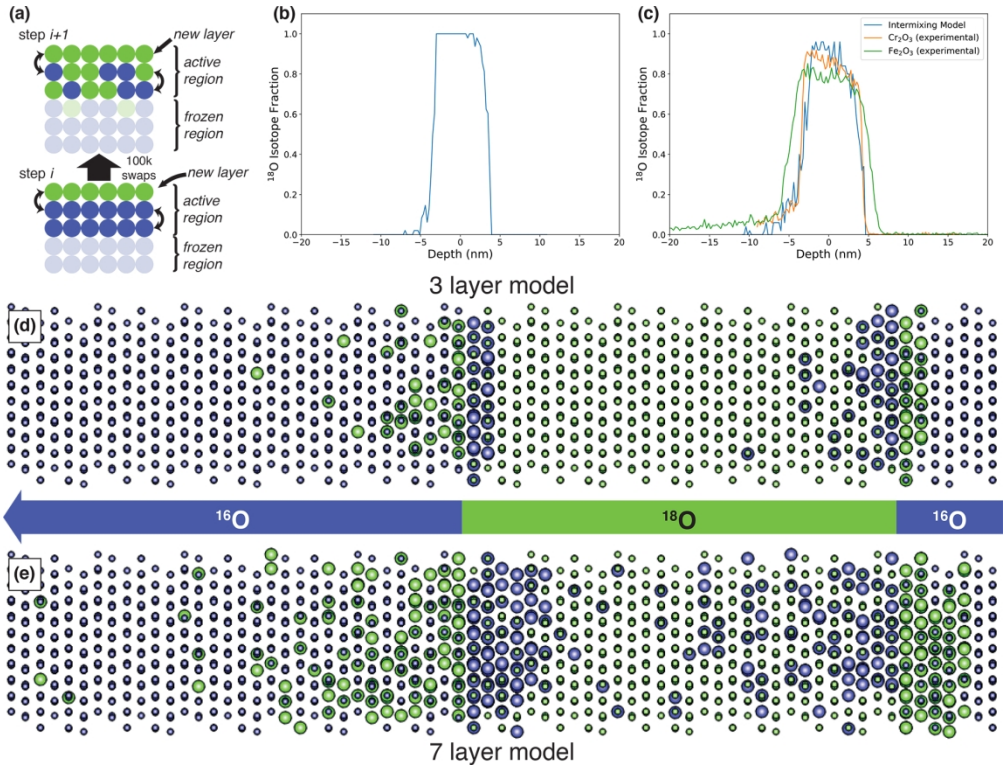

Figure 3. (a) Schematic of model mixing algorithm. As new layers are added to the growth front (after 100k swaps for the previous step), the active region (the surface and sub-surface) moves up one layer. The layers underneath are then considered frozen and all oxygen in those layers remain in place for the duration of the simulation. (b,c) ^{18}O distribution results from the model with (b) 3 layers mixing and (c) 7 layers mixing, as well as experimental ^{18}O distributions in $Fe_2O_3/Fe_2{}^{18}O_3/Fe_2O_3$ (0.1 Å/s) and $Cr_2O_3/Cr_2{}^{18}O_3/Cr_2O_3$. (d-e) The resulting atomistic profiles from the (d) 3 layer and (e) 7 layer model. Green: ^{18}O, Blue: ^{16}O. The bar indicates the isotope of oxygen that is "deposited" when a new layer is added at that point in the simulation. For clarity, larger spheres indicate atoms that mixed into a region of the other isotope, while the atoms of the deposited isotope are displayed as smaller spheres. Fe atoms are not shown.

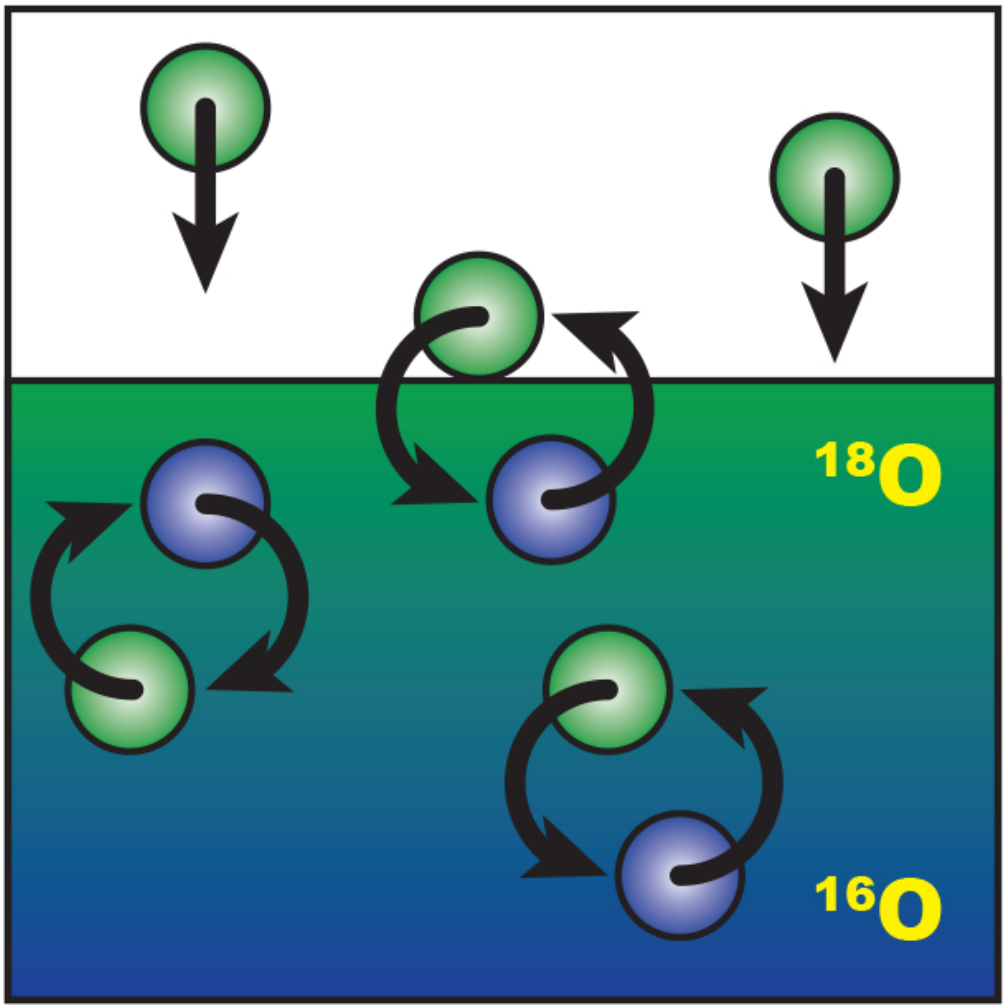
^{18}O
^{16}O